Preprints of the 21st IFAC World Congress (Virtual)
Berlin, Germany, July 12-17, 2020

Nonlinear Observer-Based Control of an Under-Actuated Hovercraft Vehicle

Lukas Pröhl * **Harald Aschemann** **

* *Chair of Mechatronics - University of Rostock*
(e-mail: lukas.proehl@uni-rostock.de)
** *Chair of Mechatronics - University of Rostock*
(e-mail: harald.aschemann@uni-rostock.de)

Abstract: This paper presents a model-based approach to the nonlinear tracking control for the body-fixed velocities of an under-actuated hovercraft vehicle. To enable a corresponding state feedback with accurate velocity signals, an observer-based sensor fusion is envisaged using acceleration measurements as well as data from an optical flux sensor. The horizontal and the vertical motion of the vehicle are modeled accordingly, and decentralized state-space representations are used for a subsequent nonlinear control design, where flatness-based techniques are employed for simplicity. To ensure steady-state accuracy, integral parts are introduced in the stabilizing feedback laws. The performance of the proposed control structure is investigated by simulation using an identified model of a corresponding experimental vehicle. In addition, also first experimental results are provided.

Keywords: Mechatronic Systems, Motion Control Systems, Modeling, Under-Actuated Vehicles, Nonlinear Observers and Filter Design, Flatness-Based Control

1. INTRODUCTION

The main objective of the current work is to design and to implement a nonlinear control for both the horizontal and vertical dynamics of a hovercraft experimental vehicle. The test rig shown in Fig. 1 was build at the Chair of Mechatronics of the University of Rostock. The hovercraft vehicle represents a demanding control application due to its nonlinear dynamics, its under-actuation as well as imperfections of the used sensor configuration.

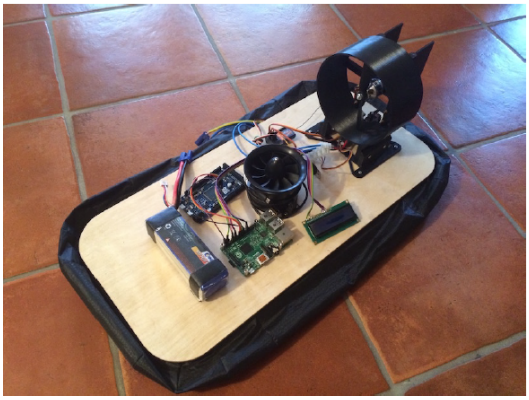

Figure 1. Photo of the hovercraft vehicle.

To reduce nonlinear friction, a pressurized air cushion is located below the vehicle, supplied by an air mass flow from a boost impeller at the center of the vehicle. For the stabilization of the vertical position of the platform, a pressure sensor is employed. The propulsion system that is predominantly used in the literature involves two fixed thrusters, see e.g. Sira-Ramírez and Ibáñez (2000a) as well as Seguchi and Ohtsuka (2002). For this kind of hovercraft vehicle, the flatness property was proven and a flatness-based control approach was designed in Sira-Ramírez and Ibáñez (2000b) to perform position tracking tasks w.r.t. the earth coordinate system. The flatness property was utilized in Sira-Ramírez (2002) as well to derive a sliding-mode position control. In the given paper, for an accurate observer-based tracking control of both the longitudinal and the lateral velocities in the body-fixed coordinate system, a propulsion propeller as well as two tiltable air blades are available.
As a precondition for feedback control, sensor data for the horizontal dynamics is provided by two independent sensor systems:

- As a first sensor system, an inertial measurement unit (IMU) is employed to measure the longitudinal and lateral accelerations as well as the yaw rate of the vehicle. Note that for measuring the yaw rate an internal compass sensor is evaluated as well to support the acceleration measurement.
- Additionally, an optical flow sensor is utilized to back up the measurement of the horizontal velocities.

As a basic pillar for the design and the implementation of the observer-based control structure, decentralized control-oriented models for the horizontal and vertical directions are derived in Sect. 2. The system parameters as well as actuator characteristics are determined by a corresponding system identification using least-squares techniques. To provide accurate estimations for the horizontal velocities in the body-fixed coordinate system – using the available measurement information of the acceleration sensor and the optical flow sensor – an observer-based sensor fusion is presented in Sect. 3. The objective of Sect. 4 is the development of a nonlinear state-observer, utilizing a quasi-linear state-space representation. Flatness-based control designs for both the horizontal as well as for the vertical dynamics are presented in Sect. 5. Simulation results and first experimental results are shown in Sect. 6. They underline

the benefits of the proposed control approach and indicate the achieved tracking accuracy.

2. MODELING OF THE SYSTEM BEHAVIOR

This section presents the derivation of a mathematical description for both the horizontal and the vertical dynamics of the hovercraft experimental vehicle. In addition to the resulting equations of motion for the vehicle itself, which are based on force and torque balances, the geometric relationships and the description of the actuator forces as well as the resulting inputs acting on the center of gravity are addressed properly.

2.1 Horizontal System Model

The model of the horizontal motion can be derived in analogy to the equations of motion for a under-actuated ship like in Aschemann and Rauh (2010), Fossen (1994) or Reyhanoglu (1997).
According to Newton's and Euler's laws of motion, corresponding force and torque balances are to be established in a body-fixed orthogonal coordinate system. For this purpose, the equations of motions are formulated first in an inertial coordinate system I and, then, transformed into the body-fixed representation.

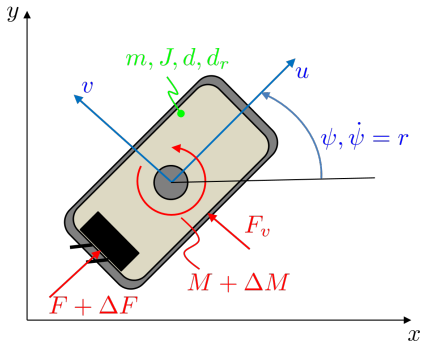

Figure 2. Mathematical model of horizontal dynamics of the hovercraft vehicle.

Given the mechanical forces acting on the hovercraft vehicle, see Fig. 2, the equation of motions in the inertial coordinate system can be stated as follows

$$m\ddot{x} + d\dot{x} = \cos(\psi)(F+\Delta F) - \sin(\psi)F_v, \tag{1}$$

$$m\ddot{y} + d\dot{y} = \sin(\psi)(F+\Delta F) + \cos(\psi)F_v, \tag{2}$$

$$J\ddot{\psi} + d_r\dot{\psi} = M + \Delta M. \tag{3}$$

A state-space representation can be established by collecting the velocities in a state vector $\underline{x}_{xy} = [\dot{x}, \dot{y}, \dot{\psi}]^T$, which results in

$$\dot{\underline{x}}_{xy} = \begin{bmatrix} \ddot{x} \\ \ddot{y} \\ \ddot{\psi} \end{bmatrix} = \begin{bmatrix} -\frac{d}{m}\dot{x} + \frac{1}{m}\left[\cos(\psi)(F+\Delta F) - \sin(\psi)F_v\right] \\ -\frac{d}{m}\dot{y} + \frac{1}{m}\left[\sin(\psi)(F+\Delta F) + \cos(\psi)F_v\right] \\ -\frac{d_r}{J}\dot{\psi} + \frac{1}{J}(M+\Delta M) \end{bmatrix}. \tag{4}$$

Here, the system parameters m and J represent the mass of the hovercraft as well as the mass moment of inertia corresponding to the orientation angle ψ. The damping coefficients d and d_r for the translational and rotatory motions characterize velocity-proportional resistances like friction and air drag. As control inputs, the acting force F as well as the torque M is considered. Additionally, a disturbance force ΔF is introduced to address external disturbances, model uncertainty as well as uncertainties of the actuator characteristics. The disturbance torque ΔM mainly addresses an additional torque caused by the uplift impeller. The disturbance force in transverse direction F_v is considered as small and will be neglected in the sequel.
The control design, however, will be based on the equations of motion within the body-fixed uv-coordinate system of the hovercraft. The corresponding coordinate transformation becomes

$$\underbrace{\begin{bmatrix} \dot{x} \\ \dot{y} \\ \dot{\psi} \end{bmatrix}}_{\underline{x}_{xy}} = \underbrace{\begin{bmatrix} \cos(\psi) & -\sin(\psi) & 0 \\ \sin(\psi) & \cos(\psi) & 0 \\ 0 & 0 & 1 \end{bmatrix}}_{\underline{R}} \underbrace{\begin{bmatrix} u \\ v \\ r \end{bmatrix}}_{\underline{x}}. \tag{5}$$

Here, the body-fixed velocities $\underline{x}$ are transformed into the velocities $\underline{x}_{xy}$ defined in the inertial coordinate system. The time derivative of $\underline{x}_{xy}$ follows from the product rule

$$\dot{\underline{x}}_{xy} = \dot{\underline{R}}\underline{x} + \underline{R}\dot{\underline{x}} \tag{6}$$

and can be solved for the time derivative of the body-fixed velocities

$$\dot{\underline{x}} = \underline{R}^{-1}\dot{\underline{x}}_{xy} - \underline{R}^{-1}\dot{\underline{R}}\underline{x}, \tag{7}$$

where the inverse transformation matrix is identical to the transposed one, i.e., $\underline{R}^{-1} = \underline{R}^T$. From (4), the force balance in the inertial x-direction can be reformulated as

$$\ddot{x} = -\frac{d}{m}\cdot\underbrace{(\cos(\psi)u - \sin(\psi)v)}_{\dot{x}} + \frac{1}{m}\cdot\cos(\psi)(F+\Delta F), \tag{8}$$

the one in y-direction follows as

$$\ddot{y} = -\frac{d}{m}\underbrace{(\sin(\psi)u + \cos(\psi)v)}_{\dot{y}} + \frac{1}{m}\cdot\sin(\psi)(F+\Delta F), \tag{9}$$

and the differential equation for the angular velocity results in

$$\ddot{\psi} = -\frac{d_r}{J}\cdot r + \frac{1}{J}\cdot(M+\Delta M). \tag{10}$$

By inserting the previous expressions into (7), a nonlinear state-space representation $\dot{\underline{x}} = \underline{f}(\underline{x}, \underline{u})$ with an affine control input can be established as follows

$$\underbrace{\begin{bmatrix} \dot{u} \\ \dot{v} \\ \dot{r} \end{bmatrix}}_{\dot{\underline{x}}} = \underbrace{\begin{bmatrix} -\frac{d}{m}u + v\cdot r \\ -\frac{d}{m}v - u\cdot r \\ -\frac{d_r}{J}r \end{bmatrix}}_{\underline{a}(\underline{x})} + \underbrace{\begin{bmatrix} \frac{1}{m} & 0 \\ 0 & 0 \\ 0 & \frac{1}{J} \end{bmatrix}}_{\underline{B}} \cdot \underbrace{\begin{bmatrix} F \\ M \end{bmatrix}}_{\underline{u}} + \underbrace{\begin{bmatrix} \frac{1}{m} & 0 \\ 0 & 0 \\ 0 & \frac{1}{J} \end{bmatrix}}_{\underline{E}} \cdot \underbrace{\begin{bmatrix} \Delta F \\ \Delta M \end{bmatrix}}_{\underline{z}}. \tag{11}$$

2.2 Geometric Characteristic of the Control Inputs

Based on the geometrical setup of the propulsion system, the acting propulsion force $F(t)$ in longitudinal direction as well as the torque $M(t)$ depend on

- the rotational speed n_p of the propulsion propeller producing the total thrust S,
- the tilt angle μ of the air blades.

The geometrical coherence to determine the force $F = F(S,\mu)$ as well as the torque $M = M(S,\mu)$ are identified by the characteristics shown in Fig. 3. The main impacts on these characteristics are the arrangement of the air blades, the diameter of the propeller, and the distance to the center of gravity.
As indicated in Fig. 4, the inverted characteristics are applied for implementing the control inputs on the hovercraft test rig.
The relationship between the rotational speed n_p and the re-

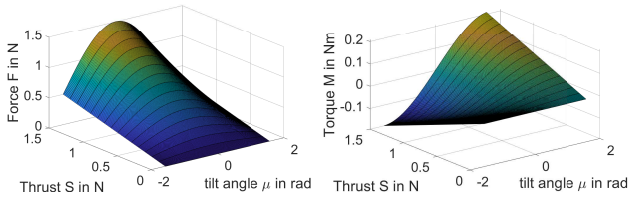

Figure 3. Force and torque characteristics $F(S,\mu)$ and $M(S,\mu)$.

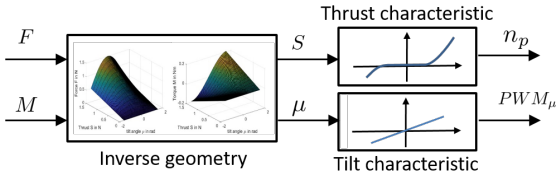

Figure 4. Implementation of the control inputs F and M at the experimental vehicle.

sulting thrust S is identified for a neutral position of the air blades, which correspond to a vanishing tilt angle. Fig. 5 shows the characteristic in forward and in backward direction. For the control of the motor of the tiltable blades, a linear characteristic is identified to describe the resulting PWM-signal (pulse-width modulation) PWM_μ for the required tilt angle.

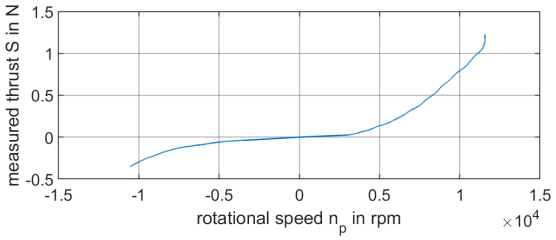

Figure 5. Identified force characteristic in forward and backward directions.

2.3 Modeling of the vertical dynamics

The vertical system model consists of the equation of motion for the hovering motion as well as a differential equation for the chamber pressure. A scheme of the design is depicted in Fig. 6.

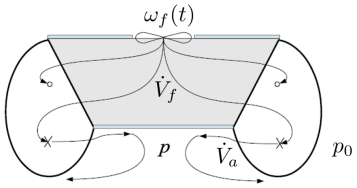

Figure 6. Mathematical model of the vertical dynamics of the hovercraft experimental vehicle.

An electrically actuated fan causes a mass flow of air that generates an overpressure in the chamber below the vehicle. The force balance in vertical direction results in

$$m\ddot{h} = (p(t) - p_0)\cdot A - m\cdot g\,. \tag{12}$$

Here, m denotes the overall vehicle mass, $p(t)$ the absolute chamber pressure, p_0 the ambient pressure, and g is the gravitation constant. The dynamics of the chamber pressure follows from a mass balance

$$\frac{d}{dt}\left(\rho(t)Ah(t)\right) = \rho(t)\left[\dot{V}_f\left(\omega_f(t)\right) - \dot{V}_a\left(h(t),p(t)\right)\right]\,, \tag{13}$$

where A is the section area, $h(t)$ denotes the lifting height, and $\rho(t)$ the density of air. The volume flow of the fan $\dot{V}_f\left(\omega_f(t)\right)$ is related to the angular velocity of the fan $\omega_f(t)$ as the outgoing volume flow out of the chamber is characterized by $\dot{V}_a\left(h(t),p(t)\right)$. Assuming an isothermal change of thermodynamic state ($\dot{\vartheta}(t)\approx 0$), the relationship between the time derivatives of pressure and density becomes

$$\dot{\rho}(t) = \frac{\dot{p}(t)}{R\vartheta(t)}\,. \tag{14}$$

Here, R stands for the gas constant of air and $\vartheta(t)$ for the temperature. This results in a differential equation for the chamber pressure

$$\dot{p}(t) = \frac{p(t)}{Ah(t)}\left[\dot{V}_f\left(\omega_f(t)\right) - \dot{V}_a\left(h(t),p(t)\right) - A\dot{h}(t)\right]\,. \tag{15}$$

The steady-state corresponds to a vanishing vertical velocity $\dot{h}(t)=0$ and leads to an identity of the steady-state volume flows according to

$$\dot{V}_{fS}(\omega_{fS}(t)) = \dot{V}_{aS}(h_S(t),p_S(t))\,. \tag{16}$$

By inverting the volume flow characteristic of the fan, a steady-state relationship between the angular velocity and the lifting height can be established

$$\omega_{fS}(t) = \underbrace{\dot{V}_{fS}^{-1}\left[\dot{V}_{aS}(h_S(t),p_S(t))\right]}_{f_\omega(h_S)}\,. \tag{17}$$

Here, the identified relationship between the steady-state pressure $\Delta p(t) = p_S(t) - p_0(t)$ and the steady-state lifting height $h_S(t)$ is used, see Fig. 7.

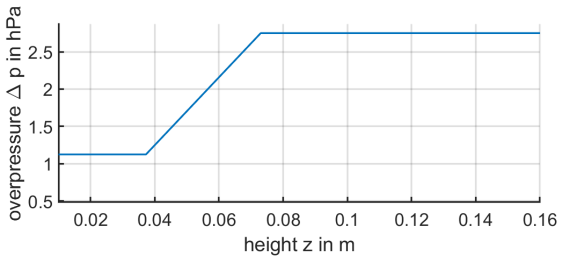

Figure 7. Identified relationship between the steady-state values of lifting height and overpressure.

3. OBSERVER BASED SENSOR FUSION

In this section, an approach for an observer-based sensor fusion is presented. Here, the same estimation technique is applicable for either of the translational velocities. The aim is to accurately determine values for the velocity $u(t)$ in longitudinal direction as well as for the velocity $v(t)$ in the lateral direction. The hovercraft vehicle is equipped with two different sensors that have to be fusioned. The first sensor is an optical flow sensor, which determines the horizontal velocities $v_{OF}(t)$ in orthogonal directions. In addition to the measured velocity $v_{OF}(t)$, this sensor delivers a feedback about the surface quality $s_q(t)$ and, hence, it allows for an assessment of the reliability of the measured signal. The measured surface quality is utilized to schedule the observer gains according to the current quality of the measurements.

As a second sensor, an multi-axes acceleration sensor is installed. To evaluate the acceleration $a(t)$, a superimposed offset $a_{off}(t)$, that is given by the IMU, has to be estimated as well. The corresponding state-space representation for the sensor combination follows as

$$\underbrace{\begin{bmatrix} \dot{v}_{OF} \\ \dot{a} \\ \dot{a}_{off} \end{bmatrix}}_{\underline{\dot{x}}_s} = \underbrace{\begin{bmatrix} 0 & 1 & 0 \\ 0 & 0 & 0 \\ 0 & 0 & 0 \end{bmatrix}}_{\underline{A}_s} \underbrace{\begin{bmatrix} v_{OF} \\ a \\ a_{off} \end{bmatrix}}_{\underline{x}_s}, \tag{18}$$

and the output equation of the two sensor signals y_{s1} and y_{s2} is given with

$$\underline{y}_s = \begin{bmatrix} y_{s1} \\ y_{s2} \end{bmatrix} = \underbrace{\begin{bmatrix} 1 & 0 & 0 \\ 0 & 1 & 1 \end{bmatrix}}_{\underline{C}_s} \underline{x}_s \,. \tag{19}$$

Consequently, the state equation for the observer becomes

$$\dot{\hat{\underline{x}}}_s = \underline{A}_s \hat{\underline{x}}_s + \underline{H}_s \left(\underline{y}_{m,s} - \underline{C}_s \hat{\underline{x}}_s \right) \,. \tag{20}$$

To determine the observer gain $\underline{H}_s$, the cost function

$$J = \int_0^\infty \left(\hat{\underline{x}}_s^T \, \underline{Q} \, \hat{\underline{x}}_s \; + \; \underline{y}_{m,s}^T \, \underline{R} \, \underline{y}_{m,s} \right) \mathrm{d}t \tag{21}$$

is minimized by solving the corresponding algebraic Riccati equation.

Note that this optimal design corresponds to a steady-state Kalman-Filter, where the matrix $\underline{Q} = \mathrm{diag}\,(q_{11}, q_{22}, q_{33}) > 0$ corresponds to the covariance matrix of the process noise, whereas the matrix $\underline{R} = \mathrm{diag}\,(r_{11}(s_q), r_{22})$ characterizes the covariance matrix w.r.t. the measurement noise, see Arulampalam et al. (2002). Here, the weight $r_{11}(s_q)$ is dependent on the measured surface quality s_q of the optical flux sensor. The schematic correspondence is depicted in Fig. 8.

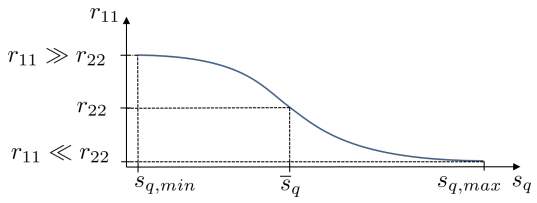

Figure 8. Weighting scheme based on the sensor quality signal.

In the case of a low surface quality ($s_q \approx s_{q,min}$), a high measurement uncertainty is applied. For an average value for the surface quality $\overline{s}_q$, the uncertainties of the sensors are balanced ($r_{11} = r_{22}$). Conclusively, the measurement uncertainty is reduced for a high surface quality ($s_q \approx s_{q,max}$).

4. QUASI-LINEAR STATE OBSERVER

In addition to the observer-based sensor fusion, a state observer is developed that allows for a smoothing and filtering of the sensor measurements. To allow for the application of an implementation of a gain-scheduled observer approach, the nonlinear and undisturbed state-space representation according to (11) will be reformulated in a quasi-linear form by introducing state-dependent matrices. Consequently, the differential equation for the state observer can be expressed as

$$\dot{\hat{\underline{x}}} = \underbrace{\underline{A}(\underline{x})\hat{\underline{x}}}_{\underline{a}(\hat{\underline{x}})} + \underline{B} \cdot \underline{u} + \underline{H}(\underline{x}) \left(\underline{y}_m - \underline{C}_m \hat{\underline{x}} \right) \,. \tag{22}$$

Here, $\underline{H}(\underline{x})$ is the state-dependent observer gain and $\underline{y}_m$ are the measured states. As all states can be measured, the measurement matrix $\underline{C}_m$ follows with $\underline{C}_m = \underline{I}$. For the observer design, the nonlinear system behaviour $\underline{a}(\underline{x})$ will be formulated utilizing a state-dependent system matrix $\underline{A}(\underline{x})$. Therefore, $\underline{a}(\underline{x})$ is given with

$$\underline{a}(\underline{x}) = \underline{A}(\underline{x}) \cdot \underline{x} = \begin{bmatrix} -\frac{d}{m} & 0 & v \\ 0 & -\frac{d}{m} & -u \\ 0 & 0 & -\frac{d_r}{J} \end{bmatrix} \cdot \begin{bmatrix} u \\ v \\ r \end{bmatrix} \,. \tag{23}$$

Now, the desired observer error dynamics can be defined by adjusting the observer gain $\underline{H}(\underline{x})$ according to

$$\underline{H}(\underline{x}) \stackrel{!}{=} \underline{A}(\underline{x}) - \mathrm{diag}\,(s_{d1}, s_{d2}, s_{d3}) \,, \tag{24}$$

where $s_{di},\ i \in \{1,2,3\}$ present the desired eigenvalues of the observer dynamics. Consequently, the observer gain $\underline{H}(\underline{x})$ becomes

$$\underline{H}(\underline{x}) = \begin{bmatrix} -s_{d1} - \frac{d}{m} & 0 & v \\ 0 & -s_{d2} - \frac{d}{m} & -u \\ 0 & 0 & -s_{d3} - \frac{d_r}{J} \end{bmatrix} \,. \tag{25}$$

For the implementation of the proposed observer approach, either the measured or the observed longitudinal and transversal velocities, i.e., u and v, may be applied for the evaluation of the observer gain.

5. FLATNESS-BASED CONTROL OF THE HORIZONTAL AND VERTICAL DYNAMICS

The main objective of this section is the nonlinear control design for the horizontal and vertical dynamics of the hovercraft vehicle. In this paper, as candidates for flat outputs in the framework of a multi-variable flatness-based control of the horizontal motion, the longitudinal velocity $y_{f1} = u$ as well as the lateral velocity $y_{f2} = v$ are considered. For the control of the vertical dynamics, the hovering height $y_{fl3} = h(t)$ of the vehicle is utilized.

Longitudinal motion The aim is to stabilize the tracking error $e_u(t) = u_d(t) - u(t)$, where $u_d(t)$ denotes the desired velocity and $u(t)$ the vehicle velocity in longitudinal direction. The first time derivative $\dot{y}_{f1} = \dot{u}$ of the flat output $y_{f1} = u$ is given by

$$\dot{u}(t) = \frac{F(t)}{m} - \frac{d}{m} u(t) + v(t) r(t) \,, \tag{26}$$

which is the first differential equation in (11). Here, the acceleration $\dot{u}(t)$ can be employed as a stabilizing control input

$$v_u(t) = \dot{u}(t) = \dot{u}_d(t) + \alpha_u \left(u_d(t) - u(t) \right) \,, \tag{27}$$

which results in an asymptotically stable first-order error dynamics

$$\dot{u}_d(t) - \dot{u}(t) + \alpha_u \cdot \left(u_d(t) - u(t) \right) = 0 \,, \tag{28}$$

where $\alpha_u > 0$ holds. The control law for the physical control input $F(t)$ becomes

$$F(t) = m \left[\dot{u}_d(t) + \alpha_u \cdot \left(u_d(t) - u(t) \right) + \frac{d}{m} u(t) - v(t) r(t) \right] \,. \tag{29}$$

Lateral motion The second control objective consists in stabilizing the lateral tracking error $e_v(t) = v_d(t) - v(t)$. The first time derivative of the lateral velocity $y_{f2}(t) = v(t)$ is given by

$$\dot{y}_{f2}(t) = \dot{v}(t) = -\frac{d}{m} v(t) - u(t) \cdot r(t) \,. \tag{30}$$

A further time differentiation leads to a dependency on the control input $M(t)$

$$\ddot{y}_{f2}(t) = -\frac{d}{m}\underbrace{\left[-\frac{d}{m}v(t) - u(t)\cdot r(t)\right]}_{\dot{v}(t)} - \dot{u}(t)\cdot r(t) - u(t)\underbrace{\left[\frac{M(t)}{J} - \frac{d_r}{J}r(t)\right]}_{\dot{r}(t)} . \tag{31}$$

Then, the physical control input $M(t)$ can be determined in a straight-forward manner

$$M(t) = J\dot{r}(t) + d_r r(t) , \tag{32}$$

with the nonlinear expressions

$$\dot{r}(t) = -\frac{1}{u(t)}\left[\upsilon_v + \dot{u}(t)\, r(t) + \frac{d}{m}\dot{v}(t)\right] , \tag{33}$$

$$\dot{v}(t) = \frac{1}{m}\left(-d\, v(t) - m\, r(t)\, u(t)\right) , \tag{34}$$

$$\dot{u}(t) = \frac{1}{m}\left(F(t) - d\, u(t) + m\, r(t)\, v(t)\right) . \tag{35}$$

Moreover, the desired closed-loop behaviour is specified by the stabilizing control law

$$\upsilon_v = \ddot{v}_d(t) + \alpha_{vd}\cdot(\dot{v}_d(t) - v(t)) + \alpha_v\cdot(v_d(t) - v(t)) + \alpha_{vI}\cdot\int_0^t((v_d(t) - v(t))d\tau , \tag{36}$$

which corresponds to a third-order error dynamics. The positive coefficients α_{vd}, α_v, and α_{vI} are chosen appropriately to obtain a Hurwitz polynomial and $v_d(t)$ and $\dot{v}_d(t)$ state the desired lateral velocity as well as the corresponding time derivative, respectively. The singularity in (33) is considered by activating this control law only for longitudinal velocities $|u(t)| \leq u_{min}$.

Vertical motion For the control design for the hovering motion, a quasi-static description of the chamber pressure can be assumed. Then, the basis of the control design is given by the equation of motion in vertical direction. Using the overpressure as a physical control input, the height represents an obvious flat output $y_{fl3} = h(t)$. The inverse dynamics follows directly as

$$\Delta p_S(t) = \frac{m(\ddot{h}(t) + g)}{A} . \tag{37}$$

The stabilizing control input is chosen as the vertical acceleration

$$\upsilon_h(t) = \ddot{h}(t) = \ddot{h}_d(t) + \alpha_{hd}\cdot(\dot{h}_d(t) - \dot{h}(t)) + \alpha_h\cdot(h_d(t) - h(t)) , \tag{38}$$

where positive coefficients $\alpha_p > 0$ and $\alpha_{hd} > 0$ must be chosen to obtain a Hurwitz polynomial. The overall control is linear and becomes

$$\Delta p_S(t) = \frac{m(\upsilon_h(t) + g)}{A} . \tag{39}$$

Note that the steady state is reflected in the identified characteristic in Fig. 7.

6. SIMULATION AND FIRST EXPERIMENTAL RESULTS

This section is dedicated to the investigation of the proposed control structure by means of both simulations and first experiments for the longitudinal motion.

6.1 Simulations of an evasive maneuver

In the sequel, simulation results are provided for an evasive maneuver in sidewards direction. In this simulation, the system model is evaluated with identified parameters and characteristics. Moreover, realistic sensor noise is considered as well. The reference trajectory involves an acceleration phase up to a forward velocity of 0.6 m/s, followed by a short sidewards motion by 0.8 m with a maximum velocity of approx. 0.3 m/s. The path in the xy-plane is illustrated in Fig. 9. Note that the velocities in the body-fixed coordinate system serve as controlled outputs. Therefore, the vehicle position is of minor importance.

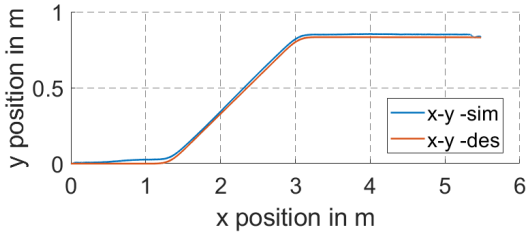

Figure 9. Reference path in the xy-plane for the hovercraft vehicle in the simulation scenario.

To reflect the disturbance torque of the boost impeller, a constant disturbance torque of $\Delta M = 0.1\,\mathrm{Nm}$ is applied. Fig. 10 shows the time behavior of the body-fixed velocities during the evasive maneuver. The simulation shows that the reference trajectories for the lateral motion are tracked quite well with small tracking errors. The reference trajectory has been defined properly to avoid a singularity in the control law (33) for the lateral motion, which corresponds to a vanishing velocity in longitudinal direction. The desired yaw rate r_{des} can be derived by utilizing the desired values for the transversal velocities u_d and v_d for the evaluation of the differential equation (11). In the current control implementation, for simplicity, a threshold u_{min} is defined above which the control is activated. Below this minimum velocity, the lateral control is deactivated. Note that this singularity can be avoided using path following instead of trajectory tracking, see De Luca et al. (2001).
The corresponding force $F(t)$ as well as the resulting torque $M(t)$ – generated by the propulsion propeller and the tiltable air blades – are depicted in Fig. 11.

6.2 First experimental results

The main objective of this subsection is to present recent experimental results from an implementation of the proposed control strategy at the hovercraft vehicle.
Fig. 12 shows a comparison of the desired and the measured velocities in longitudinal direction for a pure straight-line motion of the vehicle. As can be seen from the raw sensor signal of the optical flow measurement, this signal is quite noisy and shows large changes caused by different surface qualities. Thanks to the sensor fusion, where an additional acceleration measurement is employed to support the velocity measurement, the estimated velocity in longitudinal direction is closer to the desired values and indicates an acceptable tracking performance.
Moreover, Fig. 13 depicts the corresponding drive force and the resulting motor speed of the propulsion propeller. The acceleration phase, the segment with constant velocity and the deceleration phase are clearly reflected in the force time series.

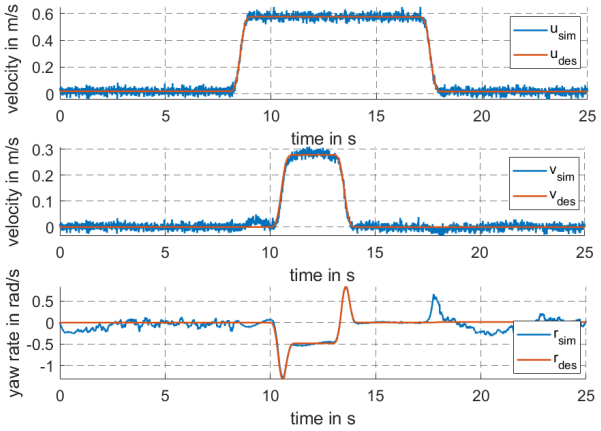

Figure 10. Simulated velocities for the control of the horizontal dynamics during the evasive reference maneuver: comparison of the desired velocity u_{des} and simulated velocity u_{sim} in longitudinal direction (upper part), comparison of the desired velocity v_{des} and simulated velocity v_{sim} in sidewards direction (middle), and comparison of the desired yaw rate r_{des} and simulated yaw rate r_{sim} (lower part).

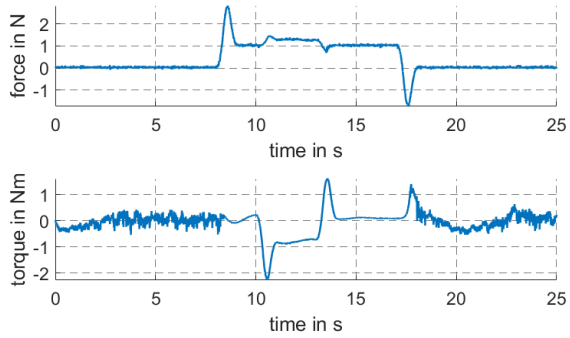

Figure 11. Simulated control inputs during the evasive maneuver.

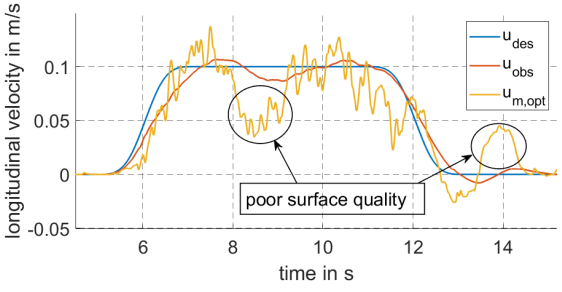

Figure 12. Experimental results for the longitudinal velocity control from an implementation on the test vehicle: desired velocity u_{des}, raw measurement signal of the optical flux sensor $u_{m,opt}$ and the observed velocity u_{obs} from the sensor fusion.

7. CONCLUSIONS AND OUTLOOK ON FUTURE RESEARCH

In this paper, a nonlinear control concept for a hovercraft vehicle is presented. The control problem is formulated in body-fixed velocities, where the reference signals are provided by the driver via a remote control. For the implementation, an observer-based sensor fusion is mandatory to obtain an acceptable signal quality. Simulation results related to an evasive maneuver indicate a good tracking behavior w.r.t. the desired velocities. Moreover, first experimental results are available for the longitudinal motion.

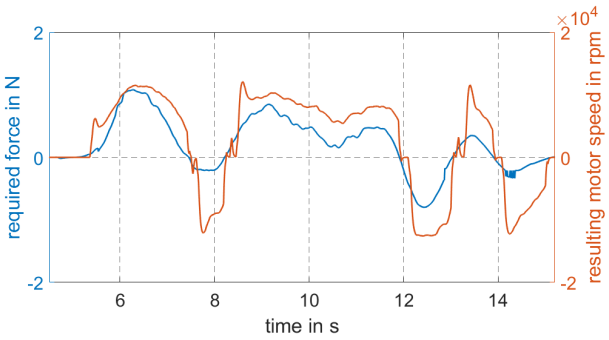

Figure 13. Applied propulsive force and motor speed of the propulsion propeller for the longitudinal motion.

In future work, especially the control performance w.r.t. the lateral and rotational degrees of freedom will be addressed in experiments on the vehicle using general desired trajectories. Furthermore, a combined trajectory planning for the horizontal motion and the applied overpressure for hovering the vehicle seem to be beneficial, because the impact of friction may be adjusted thereby in dependency on the vehicle speed.

REFERENCES

Arulampalam, M.S., Maskell, S., Gordon, N., and Clapp, T. (2002). A Tutorial on Particle Filters for Online Nonlinear/Non-Gaussian Bayesian Tracking. *IEEE Transactions on Signal Processing*, 50(2), 174–188.

Aschemann, H. and Rauh, A. (2010). Nonlinear Control and Disturbance Compensation for Underactuated Ships Using Extended Linearisation Techniques. In *8th IFAC Conference on Control Applications in Marine Systems*. Rostock-Warnemünde, Germany.

De Luca, A., Oriolo, G., and Vendittelli, M. (2001). *Lecture Notes in Control and Information Sciences*, chapter Control of Wheeled Mobile Robots: An Experimental Overview, 181–226. Springer Berlin Heidelberg.

Fossen, T.I. (1994). *Guidance and Control of Ocean Vehicles* . Chichester ; New York : Wiley.

Reyhanoglu, M. (1997). Exponential Stabilization of an Underactuated Autonomous Surface Vessel. *Automatica*, 33(12), 2249–2254.

Seguchi, H. and Ohtsuka, T. (2002). Nonlinear Receding Horizon Control of an RC Hovercraft. In *Proceedings of the International Conference on Control Applications*, volume 2, 1076–1081 vol.2. Glasgow, SmUand. U.K.

Sira-Ramírez, H. (2002). Dynamic Second-Order Sliding Mode Control of the Hovercraft Vessel. *IEEE Transactions on Control Systems Technology*, 10(6), 860–865.

Sira-Ramírez, H. and Ibáñez, C.A. (2000a). On the Control of the Hovercraft System. *Dynamics and Control*, 10(2), 151–163.

Sira-Ramírez, H. and Ibáñez, C.A. (2000b). The Control of the Hovercraft System: A Flatness Based Approach. In *Proceedings of the 2000. IEEE International Conference on Control Applications. Conference Proceedings (Cat. No.00CH37162)*, 692–697. Anchorage, Alaska, USA.